Petroleum Science 20 (2023) 1998–2008

Contents lists available at ScienceDirect

Petroleum Science

journal homepage: www.keaipublishing.com/en/journals/petroleum-science

Original Paper

Decipher hydrocarbon generation and accumulation based on fluid inclusion and chronology: A case study from the Upper Paleozoic buried-hills in Huanghua Depression, Bohai Bay Basin

Li-Hong Zhou [a], Yong Li [a, b, *], Feng-Ming Jin [a], Jin-Feng Xie [b], Xiu-Gang Pu [a], Li-Xin Fu [a], Da Lou [a], Yang Tian [b]

[a] PetroChina Dagang Oilfield Company, Tianjin, 300280, China
[b] State Key Laboratory of Coal Resources and Safe Mining and College of Geosciences and Surveying Engineering, China University of Mining and Technology, Beijing, 100083, China

ARTICLE INFO

Article history:
Received 11 February 2022
Received in revised form
4 January 2023
Accepted 15 March 2023
Available online 17 March 2023

Edited by Jie Hao and Teng Zhu

Keywords:
Petroleum accumulation
Buried hills
K–Ar isotope
Fluid inclusions
Huanghua depression
Bohai Bay Basin

ABSTRACT

Deciphering hydrocarbon generation and accumulation stage is of significance to understand oil and gas evolution and seek exploration targets. Taking the Upper Paleozoic buried-hills in the Huanghua Depression, Bohai Bay Basin, as a case study, hydrocarbon generation environment and detailed accumulation process are revealed by fluid inclusions observations, Laser Raman spectroscopy, Fourier Infrared spectroscopy, and K–Ar isotope measurements. The results show that both oil and gas inclusion were captured in the quartz overgrowth, dissolved feldspar and calcite microfractures, showing blue to dark brown fluoresce. The grains containing oil inclusions index (GOI) of oil, oil & gas and gas being 25%, 65%, and 10% and the inclusions with abundant methyl groups and short chains, both indicate high thermal maturity. One series of fluids inclusion is generally observed, evidenced by the concentrated homogenization temperature of 135–145 °C and salinity of 3%–15 w.t.% NaCl equiv, indicating one primary charging stage. The gas and gas & liquid inclusions mainly contain CH_4, with also peaks indicating CO_2 and N_2. The Carboniferous and Permian biomarkers show reducing environment with brackish water, with organic matter sources both from marine and continental. The relative content of $\alpha\alpha\alpha20RC_{27}$, $\alpha\alpha\alpha20RC_{28}$, and $\alpha\alpha\alpha20RC_{29}$ exhibit source contributions both from algae and higher plants, and mainly of II_2 to III kerogen. Both coal derived gas and oil associated hydrocarbons are identified from most of the buried-hills. Combining the fluid homogenization temperature and salinity, as well as the thermal evolution history, the hydrocarbon generated from the Upper Paleozoic was concentrated at the end of the Eocene (40 Ma±), while the beginning of charging is 60 Ma±. The Wumaying Buried-hill is of only coal derived gas and has potential for inner coal measure natural gas exploration. The results provide a detailed understanding of hydrocarbon accumulations in the study area, which can also be reference for improving petroleum exploration efficiency in similar basins.

1. Introduction

Hydrocarbon accumulation chronology becomes a frontier issue in petroleum geology recently, and an accurate estimation of accumulation time is a prerequisite to reveal the formation and distribution of oil and gas (Y. Zhang et al., 2016; Zhu et al., 2019; Wu et al., 2021). The Bohai Bay Basin, located in the east of North China Craton, is the most petroliferous basin in East China (Hao et al., 2009). Most of petroleum studies in the Bohai Bay Basin focus on the Cenozoic oil resources, while ignoring the hydrocarbon generation potential of the Paleozoic (Chang et al., 2018; Li et al., 2022). The basin is an ancient, superimposed basin with the characteristics of several depositional and erosional sequences, deeply buried reservoirs, and complicated faulted structures (Lai et al., 2019; Xu et al., 2019). The multiple source rocks, multi-stage hydrocarbon generation, and multi-stage hydrocarbon accumulation make it

* Corresponding author. PetroChina Dagang Oilfield Company, Tianjin, 300280, China.
E-mail addresses: liyong@cumtb.edu.cn, cugbliyong@gmail.com (Y. Li).

https://doi.org/10.1016/j.petsci.2023.03.010
1995-8226/

difficult to fully understand the evolution process of accumulated petroleum.

Fluid inclusions captured in the oil and gas charging stage can record the components contained therein and the temperature and pressure experienced (Steele-MacInnis et al., 2016; Chen et al., 2018). The information is effective in restoring the history of hydrocarbon charging and also accumulation characteristics (Roedder and Bodnar, 1980; Baker and Lang, 2003; Frezzotti et al., 2012; Chi et al., 2021). For immiscible trapped inclusions, the homogenization temperature of aqueous inclusions reflects the paleo geotemperature of oil and gas migration and charging. The inclusions properties can be used to determine the nature and source of the reservoir forming fluid (Wang et al., 2016; Akbulut et al., 2016; Wu et al., 2016). What's more, the hydrocarbon molecular geochemistry and light hydrocarbon isotopes is capable to reflect the petroleum sources, maturity, and genetic types (Ge et al., 2016). The isotopic characteristics of each component of natural gases can effectively identify their genetic type (Liang et al., 2021).

The Upper Paleozoic has a huge potential for petroleum development, with several wells show economical oil and gas production, in the Bohai Bay Basin. However, identification of clear targets remains a challenging task. Thus, this study was conducted with a four-fold purpose: (1) detecting single oil and gas inclusion information to reveal the temperature and pressure when oil and gas was accumulated; (2) quantifying inclusions molecular information to discuss the source of fluid inclusions; (3) determining the main accumulation period through burial history reconstruction and authigenic illite K–Ar isotopes; and (4) clarifying oil and gas sources accumulated in the buried hills by deciphering multiple sets of source rocks, multiple transport systems, and multiple reservoirs. The results are beneficial to understand the temporal and spatial variations during hydrocarbon accumulation in the Bohai Bay Basin and also provide reference for petroleum accumulation in other structured basins. And the methods, restoring hydrocarbon charging and accumulating processes from the fluid inclusion, can be useful in revealing the complicated petroleum basins evolution history.

2. Geological setting

The Bohai Bay basin is an extensional basin formed on the complex fault system of Mesozoic and Cenozoic in the eastern part of North China Craton. And the fault activity runs through the entire basin evolution (Zhao et al., 2018; Ju et al., 2021). The Huanghua Depression is located in the central part of the basin. It is a large-scale negative-trending structural unit with rich hydrocarbons (Wang et al., 2020; Yang et al., 2020). Affected by the uplift of Caledonian movement at the end of Ordovician, the Early Carboniferous strata were generally absent. The regional strata successively deposited are Meso-Neoproterozoic, Lower Paleozoic Cambrian and Ordovician, Upper Paleozoic Carboniferous Permian and Meso-Cenozoic strata. After the deposition of the Upper Paleozoic, multi-stage tectonic evolution happened during the Hercynian, Indosinian, Yanshanian and Himalayan movements. The Upper Paleozoic Carboniferous-Permian is a set of marine to continental transitional deposits, with coal related source rocks developed in the Taiyuan and Shanxi formations. The coal measure strata are thin in the north and thick in the south (Fig. 1).

3. Methodology

3.1. Samples

Samples were collected from different structural units, including the Wumaying Buried-hill, Xuhei Buried-hill, Liugangzhuang Buried-hill, Beidagang buried-hill, and Kongdian Structural-belt. All samples were collected from Carboniferous–Permian. A total of 27 samples were tested for detailed inclusion petrographic observation and analysis, homogenization temperature, and salinity tests to clarify the petroleum occurrence status and accumulations.

3.2. Fluid inclusions

Homogenization temperature and salinity tests of aqueous inclusions related to oil and gas inclusions were conducted following Goldstein (2001). Temperature measurement inclusions were 10–17 μm in diameter, with an 8% or less gas-to-liquid ratio. They were all regular-shaped hydrocarbon-bearing aqueous inclusions, thereby avoiding uneven capture and reliability of inclusions and ensuring the quality of inclusions (Pan et al., 2015). Similarly, when comparing the inclusions of brine and hydrocarbon-bearing brine, composed of brine and trace hydrocarbons (mainly CH_4), their homogenization temperature was the actual formation temperature of the inclusions. Using a Linkam THMS-G600, the homogenization temperature and salinity of the fluid inclusions were measured, and the accuracy of the uniform method was ± 1 °C.

3.3. K–Ar isotope analysis

The basic procedures for sedimentary rock clay minerals extraction and separation were as follows. First, electronic raster image analysis was performed on 500–1000 g sandstone samples, and then surface contaminants were removed and repeatedly ground to 1–2 mm. Using 500–800 g samples, oil was cleaned to remove H_2O_2, and organic matter was soaked in deionized water or distilled water. The solution was stirred or kneaded to separate the clay and make a clay suspension. Then, the precipitation method was used to remove clay minerals above 1.0 μm, and they were separated by high-speed centrifugation with pore diameters of 1–0.5, 0.5–0.3, 0.3–0.2, 0.2–0.1 ($\geq$0.1). Finally, 2–3 samples were selected from the finest grade (depending on the number of clay samples selected), and X-ray Diffraction (XRD) analysis was performed to understand the composition of clay minerals. Certain assumptions must be satisfied before the age of a rock or mineral can be calculated with the Potassium–Argon dating technique (McDougall and Harrison, 1999). The K–Ar method and its derivative, the $^{40}Ar/^{39}Ar$ method, are based on the radioactive decay of ^{40}K to the noble gas ^{40}Ar (sometimes symbolically indicated as $^{40}Ar^*$, or radiogenic Ar). An MM5400 noble gas mass-spectrometer was used to measure the isotope ratios with high resolution (Kowalska et al., 2019; Bablon et al., 2020).

3.4. Micro fourier transform infrared (Micro-FTIR)

A Nicolet 6700 NEXUS Micro-FTIR spectrometer was used to analyze the oil and gas contents. Test conditions consisted of a mercury cadmium telluride-A detector, with a scanning range of 4000–650 cm^{-1}, scanning time of 128, and resolution of 8 cm^{-1}. The measured restricted area was usually larger than 10 μm^2 to avoid streaks and improve the signal-to-noise ratio. The intensity of various infrared absorption peaks represented the relative abundance of various chemical groups, and their abundance ratio reflected the structural composition characteristics of organic matter (Chen et al., 2015). The distribution of each absorption peak was determined with the following criteria: (1) interval 3000–2947 cm^{-1} with main peak at 2960 cm^{-1} representing methyl asymmetric stretching vibration (CH_{3a}); (2) interval 2947–2883 cm^{-1} with main peak at 2930 cm^{-1} representing the asymmetric stretching vibration of the methylene group (CH_{2a}); (3)

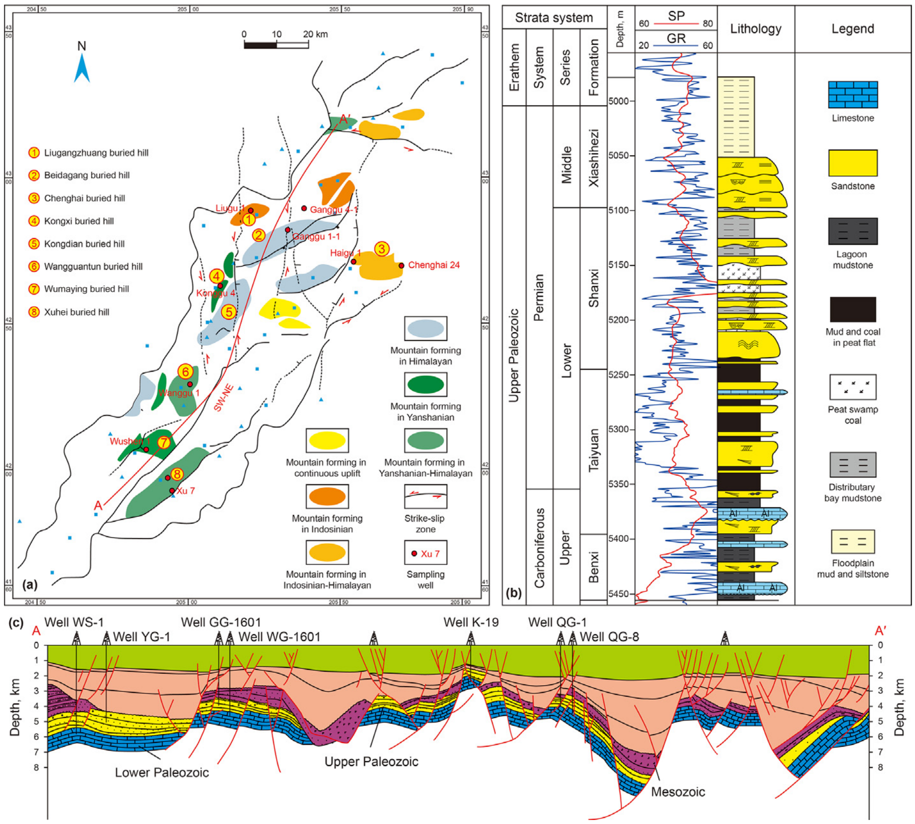

Fig. 1. Geological overview of the Huanghua Depression in the Bohai Bay Basin. (a) location of the Bohai Bay and the main buried hills developed; (b) Upper Paleozoic lithology of the Huanghua Depression; and (c) cross-sectional of the Huanghua Depression in nearly SW-NE direction.

interval 2883–2869 cm^{-1} with main peak at 2873 cm^{-1} representing the methyl symmetric stretching vibration (CH_{3s}); and (4) interval 2869–2800 cm^{-1} with main peak at 2856 cm^{-1} representing the methylene symmetric stretching vibration (CH_{2s}).

3.5. *Laser Raman spectroscopy*

A LabRAM HR800 laser Raman spectroscopy from JOBINYVON (France) was used to measure the saltwater and gaseous hydrocarbon content. Silicon wafer calibration shall be carried out before the instrument is used. The two wavelengths of the laser were used for testing. The scanning range were 100–4200 cm^{-1}, with a laser beam spot size of 1 μm±, and a spectral resolution of 2 cm^{-1} (Zhang et al., 2017). Four groups were determined by the peak areas, which were the methyl asymmetric stretching vibration (CH_{3a}), methylene asymmetric stretching vibration (CH_{2a}), methyl symmetric stretching vibration (CH_{3s}), and methylene symmetric stretching vibration (CH_{2s}).

3.6. *Gas chromatography-mass spectrometry (GC-MS)*

The hydrocarbon composition characteristics of oil and gas inclusions were tested by the combination of chemical extraction and physical fragmentation. Gas chromatography-mass spectrometry (GC-MS) analysis was performed by Agilent 6890N-5975IMSD chromatography/mass spectrometer. The chromatographic column is HP-5MS (30 m × 0.25 mm × 0.25 μm), and the sample was injected in pulse non split mode. The carrier gas was helium, and the internal standard method was used for quantification. The stable carbon isotope analysis instrument of monomer hydrocarbon is GV IsoPrime Agilent 6890N chromatography isotope mass spectrometry. Results used PDB as the standard, and the error range of stable carbon isotope determination was ±0.1‰.

4. Results

4.1. *Fluid inclusion petrography*

4.1.1. *Fluid inclusions occurrence*

Fluid inclusions are observed in the quartz, feldspar and calcite particles, which are generally being captured during the middle to late diagenetic stages. The sandstones capture light oil and bitumen in the intergranular pores and microfractures, showing dark brown fluorescent, indicating large-scale light oil and gas filling (Fig. 2a and b). For light hydrocarbons, usually one series inclusion is seen, indicating one primary charging stage. The inclusions were captured in the quartz secondary overgrowths during the middle to late diagenesis. The grains containing oil inclusions (GOI) index is approximately 15%. Some inclusions were captured in a banded or isolated states in the later authigenic calcite cements (Fig. 2c and d), or distributed in linear/banded micro-fractures cutting quartz grains (Fig. 2e and f). The inclusions can also be seen in the feldspar dissolution particles, generally in cluster or banding distribution (Fig. 2g and h). The liquid hydrocarbons in the inclusions are light yellow to dark yellow, showing strong light blue and blue-green fluorescence, and the gas hydrocarbons are kind of gray (Fig. 2c–h). By measuring the GOI values of various types of fluid inclusions, the study found that the geochemical indices of oil inclusions, oil and gas inclusions and natural gas inclusions were approximately 25%, 65% and 10%, respectively. This indicate that the hydrocarbon charging was primarily medium and light oil and gas, which is products at high mature stages.

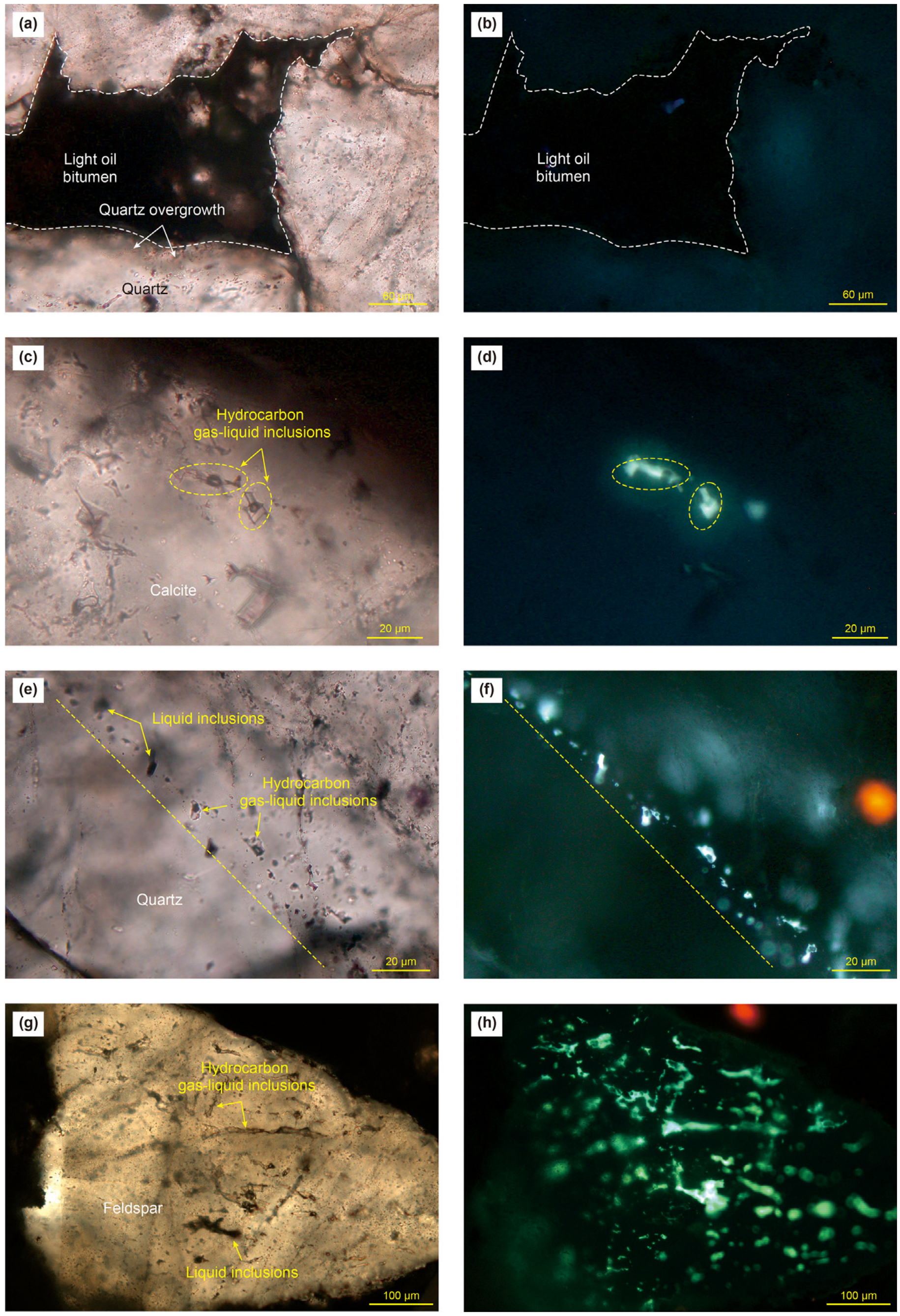

Fig. 2. Microscopic features of the fluid inclusions. (a) polarized light, P_1x, 4858.23 m; (b) Same position as (a), UV excitation fluorescence, P_1x, 4858.23 m; (c) polarized light, P_1x, 4859.8 m; (d) and (c) the same position, UV excitation fluorescence, P_1x, 4859.8 m; (e) polarized light, P_1x, 4859.14 m; (f) the same position as (e), UV excitation fluorescence, P_1x, 4859.14 m; (g) polarized light, P_1x, 4858.6 m; (h) the same position as (g); and UV excitation fluorescence, P_1x, 4858.6 m.

4.1.2. Homogenization temperature and salinity

The microscopic results show that the inclusions are mainly of one stage charging. The temperature of the hydrocarbon-bearing aqueous inclusions was tested (Fig. 3). The homogenization temperature of inclusions shows one single peak, concentrating between 135 and 145 °C. The salinity of inclusions is calculated according to Bodnar (1993), which has a wide variation range between 0 and 24 w.t.% NaCl equiv. And it should be noticed that most of salinity results are concerted in the range of 3 w.t.% to 15 w.t.% NaCl equiv. The results confirm that the inclusions are generally of one stage. At the same time, the homogenization temperature of the salinity and fluid inclusions show a single-peaked distribution, suggesting a strong tectonic thermal event.

4.2. Fluid inclusion composition

4.2.1. Laser Raman spectroscopy

The gas inclusions and gas-liquid two-phase inclusions occurred in quartz overgrowths were tested to show their composition. A peak at 2911 cm^{-1} is observed in the samples from Wumaying Buried-hill, which is speculated to be a methane peak (Fig. 4a). The gas composition was judged to be methane. There are peaks with also strong CO_2 and weak N_2 characteristic (Fig. 4c). Similarly, well HG101 in Chenghai Buried-hill, also had a peak with obvious methane characteristics (Fig. 4b), while weak CO_2 peaks occur at 1281 and 1385 cm^{-1} (Fig. 4d). Thus, apart from CH_4 captured during the geological history, there are also CO_2 and N_2 being recorded in the fluid inclusions.

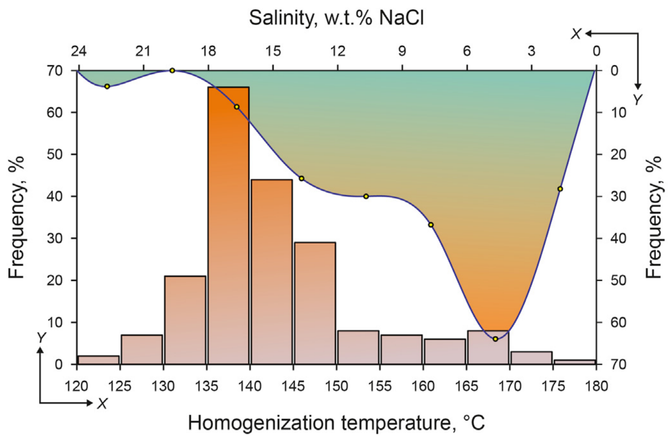

Fig. 3. Homogenization temperature and salinity distribution of hydrocarbon-bearing aqueous inclusions.

4.2.2. Micro-FTIR

The infrared spectra from different samples show distinct aliphatic hydrocarbon absorption peaks between 2800 and 3000 cm^{-1} (Table 1; Fig. 5). The methylene-to-methyl area ratio (AR) can indicate their relative abundance. The smaller the AR ratios, the higher the maturity of the organic matter in the inclusions. The absorption intensity of methylene in oil and gas inclusions is slightly greater than that of methyl, and the area ratio (AR) of methylene to methyl was less than 4.0, with only a few samples having high AR ratios. The number of carbon atoms of organic alkyl (X_{inc}) and the number of carbon atoms of standard organic alkyl (X_{std}) were mainly between 14–46 and 8–19, respectively. The results show abundance of methyl groups, short hydrocarbon chains, and the maturity is relatively high. And the result is also consistent with the above results that there is generally one stage oil accumulation.

4.3. Molecular geochemistry and isotopes of light hydrocarbons

4.3.1. Molecular geochemistry

We select sandstone samples from well WS1 for inclusion saturated hydrocarbon GC-MS analysis and analyze the biomarker characteristics (Table 2). The distribution characteristics of n-alkanes are unimodal, with a Pr/Ph value of 0.76 and no β-carotene (β-car). The relative contents of $\alpha\alpha\alpha20RC_{27}$, $\alpha\alpha\alpha20RC_{28}$, and $\alpha\alpha\alpha20RC_{29}$ steranes are distributed in a nearly an "L" pattern, in which $\alpha\alpha\alpha$20R steranes C_{27} has a higher content than C_{29}. The C_{30} rearrangement hopane/C_{29}Ts is 5.23, Ts > Tm, and contain a certain amount of gammacerane (Fig. 6).

4.3.2. Light hydrocarbon isotope geochemistry

The carbon isotopes of alkane gas were determined, and the results are shown in Table 3. Each sample has the characteristic of the $\delta^{13}C$ value of methane, its homologs increase with an increment in the carbon number, and the methane isotope value was between −47.1‰ and −34.9‰, which is typical organic gas. The ethane isotope values range from −39.5‰ to −23.3‰, of which Permian samples from well WS1 ranged from −26.5‰ to −23.3‰, whereas the Carboniferous samples from other wells range from −39.5‰ to −33.3‰. The carbon isotope distribution of propane ranges from −34.1‰ to −21.2‰, the Permian samples ranged from −25.3‰ to −21.2‰, and Carboniferous samples from −34.1‰ to −30.2‰. Combining the above characteristics with the $\delta^{13}C_1$-$\delta^{13}C_2$-$\delta^{13}C_3$ plots (Dai et al.,2014, 2016), the alkane gas in the P_{1X} inclusions in the well WS1 is coal derived gas, while the Carboniferous oil and gas inclusions in the wells LG1, KG4, and GG4-1 partly belong to oil associated gas (Fig. 7). Thus, the methane in the Wumaying Buried-hill was generated from the coal measure source rocks. However, the hydrocarbons in the Wangguantun and Beidagang Buried-hills are of mixed sources, both from coal derived and oil associated.

4.4. K–Ar isotopic dating of authigenic illite

The K–Ar dating of the finest authigenic illite represents the time of petroleum entrances and illite growth halt. The dating results of authigenic illite collected from three wells are listed in Table 4, and the average values were about 60 Ma and 61 Ma for wells WS1 and X7. The results show that the petroleum accumulation both in the Wumaying and Xuhei Buried-hills are around 60 Ma, generally happened during the Paleocene.

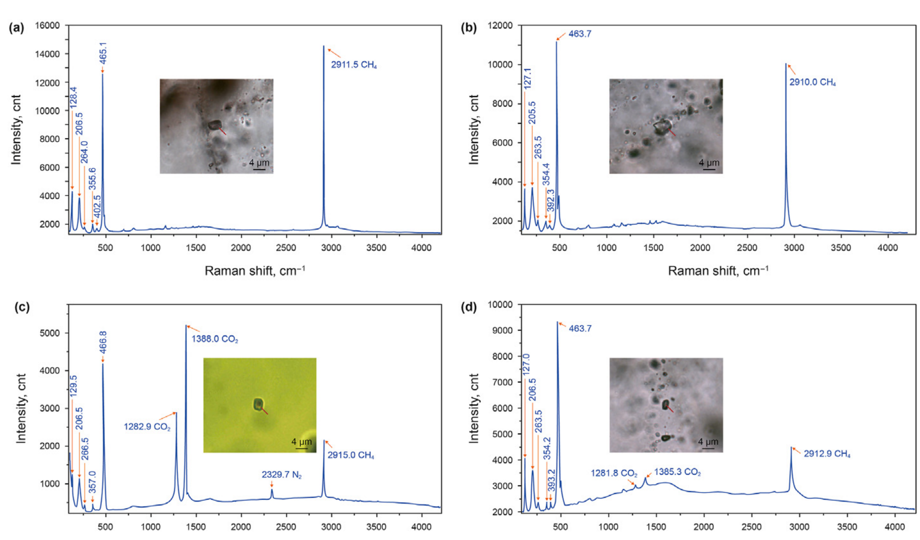

Fig. 4. Spectrum of typical Raman probe, with pictures showing the location of the measuring points. (a) methane peak from Well WS1, (b) methane peak from well HG101, (c) CO_2 and N_2 peaks from well WS1, (d) CO_2 and CH_4 peaks from well HG101.

Table 1
Microscopic Fourier infrared spectroscopic parameters of inclusions.

Location	Sample	Depth, m	Absorbance value/Eo				AR $\frac{CH_2}{CH_3}$	X_{inc}	X_{std}
			2960	2930	2873	2856			
Wumaying Buried-hill	XWK-1	4858.60	0.139	0.345	0.022	0.032	2.342	17.129	9.043
WS1	XWK-2	4858.60	0.115	0.268	0.008	0.038	2.496	18.844	9.615
	XWK-3	4858.60	0.144	0.286	0.005	0.030	2.125	14.722	8.241
	XWK-4	4859.70	1.350	3.310	0.032	0.342	2.643	20.473	10.158
	XWK-5	4859.70	0.053	0.177	0.050	0.042	2.130	14.780	8.260
	XWK-6	4859.33	0.332	0.676	0.011	0.097	2.254	16.152	8.717
	XWK-7	4859.33	0.348	0.893	0.006	0.118	2.856	22.844	10.948
	XWK-8	4857.70	0.142	0.360	0.012	0.077	2.844	22.708	10.903
	XWK-9	4857.70	0.446	1.151	0.019	0.150	2.798	22.198	10.733
	XWK-10	4857.88	0.200	0.613	0.009	0.055	3.204	26.716	12.239
	XWK-11	4857.88	0.427	0.798	0.007	0.162	2.212	15.689	8.563
	XWK-12	4858.23	0.085	0.220	0	0.031	2.950	23.884	11.295
Wuhei Buried-hill	WK-1	1300.80	0.004	0.010	0.004	0.009	2.301	16.680	8.893
X7	WK-2	1303.20	0.099	0.828	0.109	0.186	4.875	45.278	18.426
	WK-3	1303.20	0.039	0.375	0.033	0.056	6.052	58.355	22.785
Liugangzhuang-Buried-hill	W-1	3640.90	0.889	5.068	0.037	1.451	7.040	69.333	26.444
LG1	W-2	3640.90	0.438	1.242	0.017	0.238	3.253	27.253	12.418
	W-3	3641.60	0.974	1.931	0.067	0.586	2.418	17.976	9.325
	W-4	3641.60	0.884	2.561	0.066	0.771	3.507	30.082	13.361
	W-5	3641.60	0.271	0.766	0.014	0.354	3.930	34.776	14.925
	W-6	3641.60	0.401	1.467	0.013	0.493	4.734	43.714	17.905
	W-7	3641.60	0.373	1.521	0.014	0.372	4.891	45.461	18.487
	W-8	3643.80	0.789	3.941	0.039	1.112	6.103	58.918	22.973
	W-9	3643.80	0.593	3.216	0.021	0.894	6.694	65.487	25.162
Beidagang Buried-hill	K-1	1779.06	0.091	0.520	0.031	0.062	4.770	44.117	18.039
GG1-1	K-2	1779.06	0.129	0.309	0	0.058	2.845	22.722	10.907
	K-3	1779.06	0.214	0.462	0.005	0.002	2.118	14.642	8.214

$X_{inc} = (AREA[\sum CH_2]/AREA[\sum CH_3]-0.8)/0.09$; $X_{std} = (AREA\ [\sum CH_2]/AREA[\sum CH_3]+0.1)/0.27$.

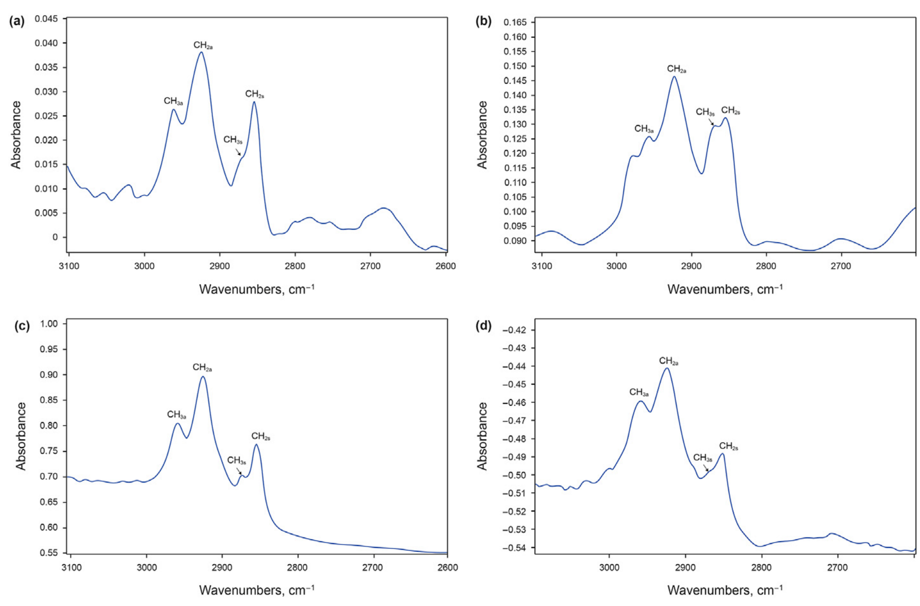

Fig. 5. Micro-FTIR spectrum of oil and gas inclusions in the middle and late stages of sandstone. Characteristic spectrum numbered (a) XWK-2, (b) WK-3, (c) X-4, and (d) K-2.

5. Discussion

5.1. Source rocks identification

The organic and inorganic geochemical characteristics of the source rocks, such as the parent material, sedimentary environment, and maturity, determine the biomarkers complexity of the source rock and its derived oil and gas (Farrimond et al., 2015; Moldowan et al., 2015; El Diasty et al., 2016). For samples from Permian, the relative content of ααα20RC_{27}, ααα20RC_{28}, and ααα20RC_{29} exhibited a nearly “L” distribution. The content of ααα20R sterane C_{27} is higher than that of C_{29}, indicating that the contribution of algae was greater than that of higher plants (El Diasty et al., 2016). The C_{30} rearrangement hopan/C_{29} Ts is 5.23, with Ts > Tm and a certain amount of gammacerane, indicating a brackish water environment. The maturity parameter Ts/(Ts + Tm) ratio is approximately 0.69, the value of C_{29} sterane ααα20S/(20S + 20R) is approximately 0.39, and the C_{29} sterane ββ/(ββ+αα) is approximately 0.52, indicating that the petroleum in this period is mature (El Diasty et al., 2016). The C_{27}/(C_{27}+C_{28}+C_{29}) ratio in the

Table 2
Parameters of the main biomarker compounds in Well WS1.

Biomarkers	Quantitative ion	Molecular weight	Retention time, min	Peak area, mv·min	Peak height, mv
Pr	TIC	268	29.307	27683886	599710
Ph	TIC	282	32.857	36426166	986266
β-car	125	558	/	/	/
Ts	191	370	63.168	36259	1012
Tm	191	370	64.086	15750	334
C_{29}H	191	398	66.987	107782	2388
C_{29}Ts	191	398	67.133	16083	444
C_{30}DH	191	412	67.390	84142	2419
C_{30}H	191	412	68.824	96798	2065
Ga	191	412	72.015	35585	542
ααα20RC_{27}	217	372	62.283	14647	341
ααα20RC_{28}	217	386	64.713	10915	184
ααα20SC_{29}	217	400	65.307	7131	168
αββ20RC_{29}	217	400	65.699	12369	256
ααα20RC_{29}	217	400	66.662	11233	240

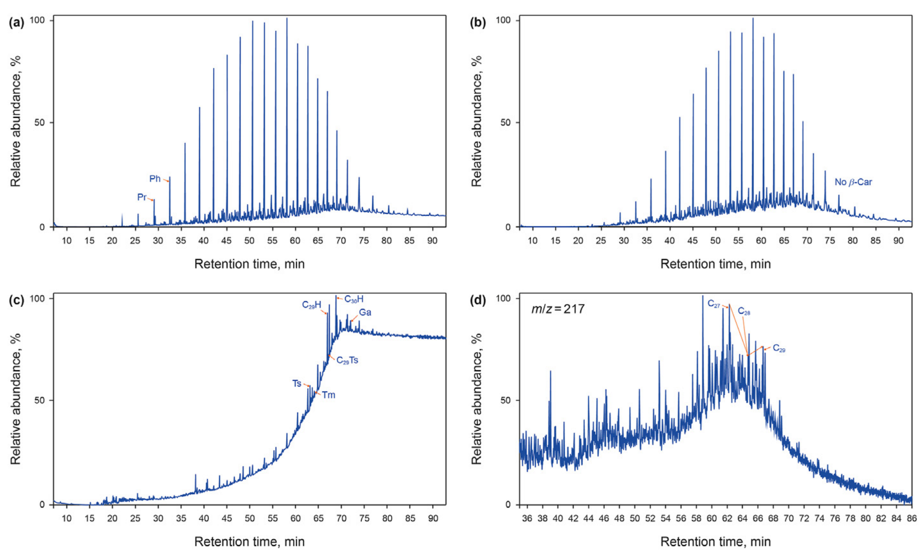

Fig. 6. Mass chromatogram of biomarkers of oil and gas inclusions. (a) Total ion current chromatogram; (b) mass-to-charge ratio, m/z = 125; (c) mass-to-charge ratio, m/z = 191; and (d) mass-to-charge ratio, m/z = 217.

Table 3
Carbon isotopic composition of alkane gas.

Well	Sample	Depth, m	Horizon	$\delta^{13}C_1$, ‰	$\delta^{13}C_2$, ‰	$\delta^{13}C_3$, ‰	$\delta^{13}C_4$, ‰	$\delta^{13}iC_4$, ‰	$\delta^{13}C_5$, ‰	$\delta^{13}iC_5$, ‰
WS1	XK-1	4857.54m	P_1x	−35.0	−26.5	−25.3	/	/	/	/
	XK-2	4857.88m	P_1x	−35.5	−23.5	−22.8	/	/	/	/
	XK-3	4858.83m	P_1x	−34.9	−24.4	/	/	/	/	/
	XK-4	4859.14m	P_1x	−35.6	−23.3	−21.2	/	/	/	/
	XK-5	4859.40m	P_1x	−35.6	−24.0	/	/	/	/	/
	XK-6	4858.60m	P_1x	−35.0	−24.1	−22.9	/	/	/	/
LG1	XK-7	3641.60m	C	−45.6	−33.4	−30.9	−29.8	/	−28.0	/
	XK-8	3643.80m	C	−45.8	−33.3	−30.2	−29.1	−31.2	−29.1	−29.8
KG4	XK-9	3810.31m	C	−47.1	−35.3	−30.5	−26.9	−28.6	−27.2	−28.6
GG4-1	XK-10	2185.90m	C	−45.0	−39.5	−34.1	−28.1	−34.3	−31.3	−31.4

oil and gas inclusions is between 39% and 40%, and C_{29}/(C_{27}+C_{28}+C_{29}) of 30% and 31%, indicating II_2 kerogen.

For the Carboniferous samples, the distribution of n-alkanes in the Xuhei Buried-hill is bimodal, while the other buried-hills are unimodal. The Pr/Ph values of each buried-hill are 0.30–1.81, indicating that oil and gas are mainly formed in a reducing to weak reducing environment (Baban and Ahmed, 2008). The samples all contain a certain amount of β-carotene, indicating that the sedimentary environment has high salinity. The relative content of ααα20RC_{27}, ααα20RC_{28}, and ααα20RC_{29} showed a "V" or nearly "V" distribution, showing that the contribution of algae was equal or slightly higher than the higher plants. The Ts/(Ts + Tm) ratios are between 0.11 and 0.76, the C_{29} sterane ααα20S/(20S + 20R) of 0.38–0.45, and C_{29} sterane ββ/(ββ+αα) of 0.35–0.59, all in the mature stage. It can be seen from Fig. 8 that the samples are influenced by the open sea and gulf environment (Fig. 8). The C_{27}/(C_{27}+C_{28}+C_{29}) value is between 35%–44%, and C_{29}/(C_{27}+C_{28}+C_{29}) is between 30 and 45%. The parent material type was type II_2 or

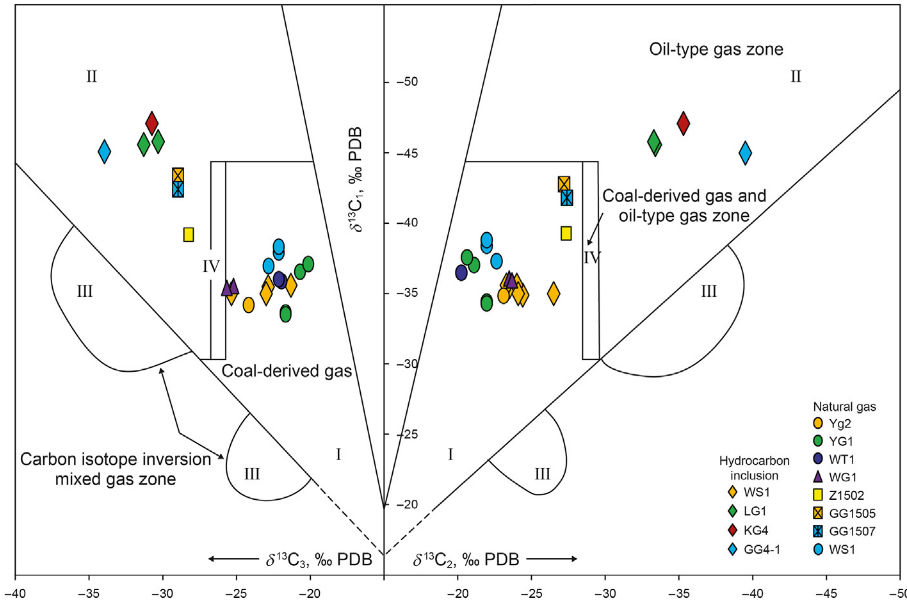

Fig. 7. $\delta^{13}C_1$-$\delta^{13}C_2$-$\delta^{13}C_3$ identification diagram of alkane gas of different areas (Diagram refer to Dai et al., 2016).

Table 4
K–Ar isotopic dating data of authigenic illite.

Well	Sample	Sample weight, g	K, %	$(^{40}Ar/^{38}Ar)_m$	$(^{38}Ar/^{36}Ar)_m$	$(^{40}Ar^{rad}/g)$ mol/g	$(^{40}K/g)$ mol/g	$^{40}Ar^{rad}/^{40}Ar^{total}$(%)	$^{40}Ar^{rad}/^{40}K$	Age(Ma,1σ)
WS1	WKX-1	0.01139	3.59	1.1433673	703.00372	4.14E-10	1.07E-07	65.6902337	0.0038580	65.21 ± 1.38
	WKX-2	0.00925	4.05	0.8929291	1348.41337	4.61E-10	1.21E-07	78.6708389	0.0038145	64.48 ± 1.33
	WKX-3	0.01285	4.79	1.1067613	1887.43341	4.75E-10	1.43E-07	88.0976053	0.0033222	56.29 ± 0.93
X7	WKX-4	0.01252	3.17	0.7892304	2058.92497	3.38E-10	9.46E-08	85.4982220	0.0035692	60.41 ± 2.00
	WKX-5	0.01352	3014	3.1090079	740.59802	3.21E-10	9.37E-08	87.1880113	0.0034286	58.06 ± 1.15
	WKX-6	0.01158	2.56	4.4021842	111.33605	2.82E-10	7.64E-08	93.521838	0.0036933	62.47 ± 2.36
	WKX-7	0.01141	1.78	3.5628930	1871.42817	2.06E-10	5.31E-08	95.3087852	0.0038792	65.56 ± 1.42

transition type II_2 to type III. Thus, compared to its upon Permian strata, the source rock in the Carboniferous is also influenced by the marine sediments.

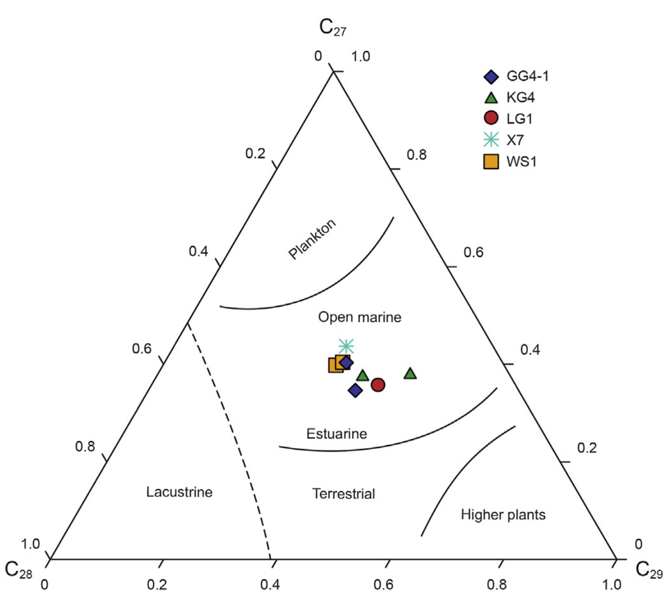

Fig. 8. Ternary plots of C_{27}, C_{28}, and C_{29} regular steranes in oil and gas inclusions (Modified from Shanmugam (1985)).

5.2. Thermal maturity

The compositional characteristics and physicochemical properties of fluid inclusions are a record of oil and gas migration and are of great importance for identifying the evolution and migration mechanisms. The Raman results show that the gases in the Wumaying and Chenghai Buried-hills are mainly of CH_4, mixed with a small amount of CO_2. The isotope results confirm that the natural gas in the Wumaying Buried-Hill is coal derived, from Upper Paleozoic coal measures (Dai et al., 2016). Except for the Wumaying Buried-Hill, all the other buried hills contain oil associated gas. The smaller the AR of the Fourier infrared spectroscopy, the higher the maturity of the organic matter in the inclusions. By establishing a X_{inc}–X_{std} identification chart (Dai et al., 2016, Fig. 9), the maturity of the inclusions was identified. The results show that the inclusions in Well WS1 are relatively rich in methyl groups and short in carbon chains, indicating that the oil and gas evolution is highly mature. In contrast, other buried hills are relatively rich in methyl groups and have shorter carbon chains, which are medium to high mature.

5.3. Petroleum accumulation time

For an oil and gas system, its critical moment contains the hydrocarbon generation and the accumulation time (Zhang et al., 2016). Fluorescence observation of fluid inclusions shows that there was a certain amount of bitumen and a small amount of light

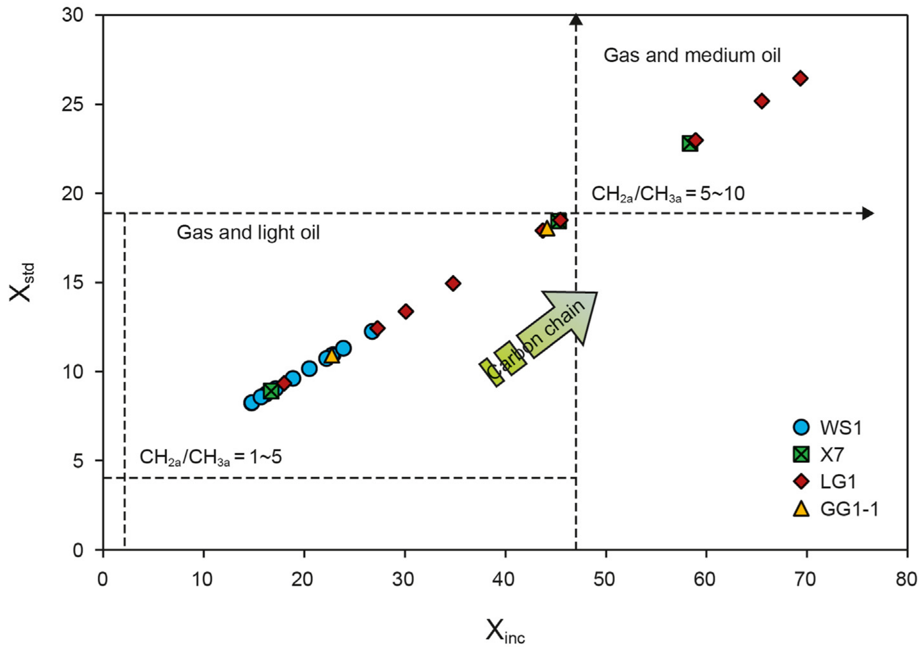

Fig. 9. X_{inc}-X_{std} oil and gas evolution maturity model (Diagram refer to Dai et al., 2016).

oil and gas, indicating that at least one stage of hydrocarbon charging occurred with diversified hydrocarbon forms (Fig. 2). According to the inclusion's occurrence, they are the residue of oil and gas migration, which happened at the late stages of the diagenesis. One main oil and gas charging stage is clearly distinguished, and they are the results at high mature stages. Thus, combining the fluid homogenization temperature and salinity, as well as the thermal evolution history, the petroleum accumulation is happened around 40 Ma and continuously to present.

However, for a continuous charging process for hydrocarbon fluids, oil and gas inclusions mainly record the early and mid-term accumulation processes, which cannot reflect the geological age of the earliest oil and gas injection. The organic matter reached a mature stage and began to generate hydrocarbons. With an increment in the charging amount, the pore water was removed, the original water-rock interaction system was destroyed, and the self-generating conversion of illite stopped. Through the K–Ar isotope age test of authigenic illite, the age value obtained was similar to the period when the oil and gas were firstly entered (Fig. 10). The Wumaying Buried-hill contain source rock with thermal maturity reaches 1.0–1.6%R_o, which has good hydrocarbon generation conditions (Zhao et al., 2018). The isotope of the inclusions shows that the natural gas type is coal-type, which is inferred to be the product of Carboniferous to Permian coal measure source rock. The strata are deposited with thick layers of dark mudstone and oil shale in Eocene, which can be good cap rocks. The Mesozoic and Cenozoic tectonic activities were frequent in the Bohai Bay Basin, while the fault generally go through the pre-Tertiary strata (Chang et al., 2018; Ju et al., 2021). Thus, the Wumaying Buried-hills is favorable for the accumulation and preservation of retained oil and gas within the Upper Paleozoic.

5.4. Implications for restoring hydrocarbon accumulation

The above results and discussion show that the detailed hydrocarbon accumulation process can be revealed by a series of measurement combining fluid inclusions, Laser Raman and Fourier infrared spectroscopies, and K–Ar isotopes. The hydrocarbon accumulation information is stored in the oil and gas inclusions and quantitatively analyzing the inclusions' molecular information cannot only give information on the source rocks and also the diagenesis environment. Combining burial history modeling and authigenic illite K–Ar isotopes, the hydrocarbon charging period can be acquired. A combination of the tests and analysis can be of significance in revealing hydrocarbon migration underground, and also helpful in understanding the geological evolution of the whole basin.

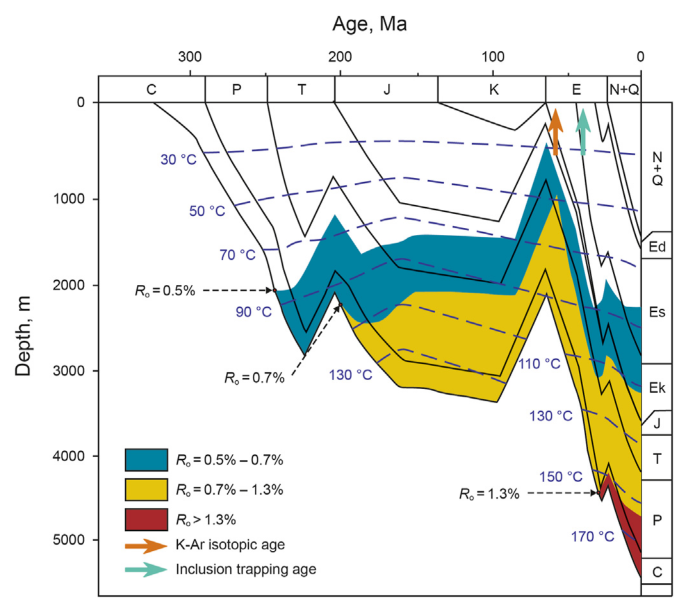

Fig. 10. Chronological diagram of oil and gas accumulation in Well WS1.

6. Conclusions

(1) Both oil and gas inclusion are captured in the quartz overgrowth, dissolved feldspar and calcite microfractures, showing blue to dark brown fluoresce. The grains containing oil inclusions index of oil, oil & gas and gas are 25%, 65%, and 10%, respectively, indicating medium to high thermal maturity. Commonly one series of fluids inclusion is observed, evidenced by the concentrated homogenization temperature of 135–145 °C and salinity of 3%–15 w.t.% NaCl equiv, indicating one primary charging stage.

(2) The gas and gas & liquid inclusions mainly contain methane, with also peaks indicating CO_2 and N_2. The Fourier infrared spectrum show that the hydrocarbons are of high mature, confirming one stage accumulation. Both Carboniferous and Permian biomarkers show reducing environment with brackish water. The relative content of $\alpha\alpha\alpha$20RC$_{27}$, $\alpha\alpha\alpha$20RC$_{28}$, and $\alpha\alpha\alpha$20RC$_{29}$ exhibit source contributions both from algae and higher plants, and mainly of II$_2$ to III kerogen.

(3) Both coal derived gas and oil associated hydrocarbons are identified from most of the buried-hills. The hydrocarbon accumulation from Upper Paleozoic source rocks was concentrated at the end of the Eocene (40 Ma±), while the beginning of petroleum charging is 60 Ma±. The Wumaying Buried-hill is of only coal derived gas and has potential for inner coal measure natural gas exploration.

Declaration of competing interest

The authors declare that they have no known competing financial interests or personal relationships that could have appeared to influence the work reported in this paper.

Acknowledgment

This study was supported by the National Natural Science Foundation of China (Grant No. 42072194, U1910205), the Fundamental Research Funds for the Central Universities (800015Z1190, 2021YJSDC02).

References

Akbulut, M., Oyman, T., Çiçek, M., et al., 2016. Petrography, mineral chemistry, fluid inclusion microthermometry and Re–Os geochronology of the Küre volcanogenic massive sulfide deposit (Central Pontides, Northern Turkey). Ore Geol. Rev. 76, 1–18. https://doi.org/10.1016/j.oregeorev.2016.01.002.

Baban, D., Ahmed, S., 2008. Biomarker Indicators of Source and Depositional Environment for the Organic Matters within Barsarin Formation (Upper Jurassic) in Kirkuk and Taq Taq Oil Fields, Northern Iraq, vol. 3. Kirkuk University Journal-Scientific Studies. https://doi.org/10.32894/kujss.2008.41950.

Bablon, M., Quidelleur, X., Siani, G., et al., 2020. Glass shard K-Ar dating of the Chalupas caldera major eruption: main Pleistocene stratigraphic marker of the Ecuadorian volcanic arc. Quat. Geochronol. 57, 101053. https://doi.org/10.1016/j.quageo.2020.101053.

Baker, T., Lang, J.R., 2003. Reconciling fluid inclusion types, fluid processes, and fluid sources in skarns: an example from the Bismark Deposit, Mexico. Miner. Deposita 38, 474–495. https://doi.org/10.1007/s00126-002-0306-3.

Bodnar, R.J., 1993. Revised equation and table for determining the freezing point depression of H2O-Nacl solutions. Geochem. Cosmochim. Acta 57, 683–684. https://doi.org/10.1016/0016-7037(93)90378-A.

Chang, J., Qiu, N., Zhao, X., et al., 2018. Mesozoic and Cenozoic tectono-thermal reconstruction of the western Bohai Bay Basin (East China) with implications for hydrocarbon generation and migration. J. Asian Earth Sci. 160, 380–395. https://doi.org/10.1016/j.jseaes.2017.09.008.

Chen, Y.Y., Zou, C.N., Mastalerz, M., et al., 2015. Applications of micro-fourier transform infrared spectroscopy (FTIR) in the geological sciences—a review. Int. J. Mol. Sci. 16, 30223–30250. https://doi.org/10.3390/ijms161226227.

Chen, L.L., Ni, P., Li, W.S., et al., 2018. The link between fluid evolution and vertical zonation at the Maoping tungsten deposit, Southern Jiangxi, China: fluid inclusion and stable isotope evidence. J. Geochem. Explor. 192, 18–32. https://doi.org/10.1016/j.gexplo.2018.01.001.

Chi, G., Diamond, L.W., Lu, H., et al., 2021. Common problems and pitfalls in fluid inclusion study: a review and discussion. Minerals-Basel 11, 7. https://doi.org/10.3390/min11010007.

Dai, J., Yu, C., Huang, S., et al., 2014. Geological and geochemical characteristics of large gas fields in China. Petrol. Explor. Dev. 41, 1–13. https://doi.org/10.1016/S1876-3804(14)60001-X.

Dai, J., Ni, Y., Huang, S., et al., 2016. Secondary origin of negative carbon isotopic series in natural gas. J. Nat. Gas. Geosci. 1, 1–7. https://doi.org/10.1016/j.jnggs.2016.02.002.

El Diasty, W Sh, El Beialy, S.Y., Mahdi, A.Q., et al., 2016. Geochemical characterization of source rocks and oils from northern Iraq: insights from biomarker and stable carbon isotope investigations. Mar. Petrol. Geol. 77, 1140–1162. https://doi.org/10.1016/j.marpetgeo.2016.07.019.

Farrimond, P., Naidu, B.S., Burley, S.D., et al., 2015. Geochemical characterization of oils and their source rocks in the Barmer Basin, Rajasthan, India. Petrol. Geosci. 301–321. https://doi.org/10.1144/petgeo2014-075.

Frezzotti, M.L., Tecce, F., Casagli, A., 2012. Raman spectroscopy for fluid inclusion analysis. J. Geochem. Explor. 112, 1–20. https://doi.org/10.1016/j.gexplo.2011.09.009.

Ge, X., Shen, C., Selby, D., et al., 2016. Apatite fission-track and Re-Os geochronology of the Xuefeng uplift, China: temporal implications for dry gas associated hydrocarbon systems. Geology 44, 491–494. https://doi.org/10.1130/g37666.1.

Goldstein, R.H., 2001. Fluid inclusions in sedimentary and diagenetic systems. Lithos 55, 159–193. https://doi.org/10.1016/S0024-4937(00)00044-X.

Hao, F., Zhou, X., Zhu, Y., et al., 2009. Mechanisms for oil depletion and enrichment on the shijiutuo uplift, Bohai Bay Basin, China. AAPG. Bull. (Arch. Am. Art) 93, 1015–1037. https://doi.org/10.1306/04140908156.

Ju, Y., Yu, K., Wang, G., et al., 2021. Coupling response of the Meso–Cenozoic differential evolution of the North China Craton to lithospheric structural transformation. Earth Sci. Rev. 223, 103859. https://doi.org/10.1016/j.earscirev.2021.103859.

Kowalska, S., Artur Wójtowicz Halas, S., Wemmer, K., et al., 2019. Thermal history of Lower Palaeozoic rocks from the East European Platform margin of Poland based on K-Ar age dating and illite-smectite palaeothermometry. Ann. Soc. Geol. Pol. 89. https://doi.org/10.14241/asgp.2019.21.

Lai, J., Pang, X., Xu, F., et al., 2019. Origin and formation mechanisms of low oil saturation reservoirs in Nanpu Sag, Bohai Bay Basin, China. Mar. Petrol. Geol. 110, 317–334. https://doi.org/10.1016/j.marpetgeo.2019.07.021/.

Li, Y., Pan, S., Ning, S., et al., 2022. Coal measure metallogeny: metallogenic system and implication for resource and environment. Sci. China Earth Sci. 65, 1211–1228. https://doi.org/10.1007/s11430-021-9920-4.

Liang, X., Liu, S.G., Wu, L.L., et al., 2021. Early paleozoic extension-compression transition and formation of a paleo-oil reservoir system in the NW sichuan basin: implications for deeply buried hydrocarbon accumulation. Geofluids 2021, 1–25. https://doi.org/10.1155/2021/5538174.

McDougall, I., Harrison, T.M., 1999. Geochronology and Thermochronology by the 40Ar/39Ar Method. Oxford University Press, USA.

Moldowan, J.M.M., Dahl, J., Zinniker, D., et al., 2015. Underutilized advanced geochemical technologies for oil and gas exploration and production-1. The diamondoids. J. Petrol. Sci. Eng. 126, 87–96. https://doi.org/10.1016/j.petrol.2014.11.010.

Pan, J., Sun, T., Hou, Q., et al., 2015. Examination of the formation phases of coalbed methane reservoirs in the Lu'an mining area (China) based on a fluid inclusion analysis and Ro method. J. Nat. Gas Sci. Eng. 22, 73–82. https://doi.org/10.1016/j.jngse.2014.11.018.

Roedder, E., Bodnar, R.J., 1980. Geologic pressure determinations from fluid inclusion studies. Annu. Rev. Earth Planet Sci. 8, 263–301. https://doi.org/10.1146/annurev.ea.08.050180.001403.

Shanmugam, G., 1985. Significance of coniferous rain forests and related organic matter in generating commercial quantities of oil, Gippsland Basin, Australia. AAPG (Am. Assoc. Pet. Geol.) Bull. 69, 1241–1254. https://doi.org/10.1306/AD462BC3-16F7-11D7-8645000102C1865D.

Steele-Macinnis, M., Ridley, J., Lecumberri-Sanchez, P., et al., 2016. Application of low-temperature microthermometric data for interpreting multicomponent fluid inclusion compositions. Earth Sci. Rev. 14–35. https://doi.org/10.1016/j.earscirev.2016.04.011.

Wang, P., Liu, S., Shen, Z., et al., 2016. Geochemical characteristics of natural gas in the hydrocarbon accumulation history, and its difference among gas reservoirs in the Upper Triassic formation of Sichuan Basin, China. J. Nat. Gas. Geosci. 1, 277–286. https://doi.org/10.1016/j.jnggs.2016.10.002.

Wang, J., Guan, Z., Croix, A.L., et al., 2020. Seismic geomorphology of shallow-water lacustrine deltas in the Paleocene Huanghua depression, Bohai Bay Basin, eastern China. Mar. Petrol. Geol. 120. https://doi.org/10.1016/j.marpetgeo.2020.104561.

Wu, J., Liu, S., Wang, G., et al., 2016. Multi-stage hydrocarbon accumulation and formation pressure evolution in sinian dengying formation-cambrian longwangmiao formation, gaoshiti-moxi structure, sichuan basin. J. Earth Sci. 27, 835–845. https://doi.org/10.1007/s12583-016-0706-4.

Wu, L., Jin, Z., Liu, K., et al., 2021. Evolution of a deeply-buried oil reservoir in the north Shuntuoguole Low Uplift, Tarim Basin, western China: insights from molecular geochemistry and Re–Os geochronology. Mar. Petrol. Geol. 134, 105365. https://doi.org/10.1016/j.marpetgeo.2021.105365.

Xu, S., Hao, F., Xu, C., et al., 2019. Hydrocarbon migration and accumulation in the northwestern bozhong subbasin, Bohai Bay Basin, China. J. Petrol. Sci. Eng. 172, 477–488. https://doi.org/10.1016/j.petrol.2018.09.084.

Yang, R., Zhao, X., Li, H., et al., 2020. Evolution characteristics of the upper Paleozoic

source kitchen and its controlling effects on hydrocarbon accumulation in the Paleozoic petroleum system in Huanghua Depression, Bohai Bay Basin, China. J. Petrol. Sci. Eng. 193, 107415. https://doi.org/10.1016/j.petrol.2020.107415.
Zhang, Y., Liu, K., Luo, X., 2016. Evaluation of 40Ar/39Ar geochronology of authigenic illites in determining hydrocarbon charge timing: a case study from the silurian bituminous sandstone reservoirs, tarim basin, China. Acta. Geol. Sin-Engl. 90, 684–703. https://doi.org/10.1111/1755-6724.12698.
Zhang, Q., Jin, W.J., Wang, J.R., et al., 2016. Relationship between magma-thermal field and hydrocarbon accumulation. Prog. Geophys. 31, 1525–1541. https://doi.org/10.6038/pg20160416.
Zhang, X., Du, Z., Zheng, R., et al., 2017. Development of a new deep-sea hybrid Raman insertion probe and its application to the geochemistry of hydrothermal vent and cold seep fluids. Deep-Sea. Res. Pt. I. 123, 1–12. https://doi.org/10.1016/j.dsr.2017.02.005.
Zhao, X., Zhou, L., Pu, X., et al., 2018. Hydrocarbon-generating potential of the upper paleozoic section of the Huanghua depression, Bohai Bay Basin. China. Energ. Fuel. 32, 12351–12364. https://doi.org/10.1021/acs.energyfuels.8b03159.
Zhu, G., Milkov, A.V., Zhang, Z., et al., 2019. Formation and preservation of a giant petroleum accumulation in superdeep carbonate reservoirs in the southern Halahatang oil field area, Tarim Basin, China. AAPG. Bull. (Arch. Am. Art) 103, 1703–1743. https://doi.org/10.1260/0144-5987.31.3.429.